



Mode I fracture toughness maximization of low-density architected materials

Holm, Markus G.; Poullos, Konstantinos; Aage, Niels; Niordson, Christian F.; Sigmund, Ole

Published in:
International Journal of Solids and Structures

Link to article, DOI:
[10.1016/j.ijsolstr.2026.113910](https://doi.org/10.1016/j.ijsolstr.2026.113910)

Publication date:
2026

Document Version
Publisher's PDF, also known as Version of record

[Link back to DTU Orbit](#)

Citation (APA):
Holm, M. G., Poullos, K., Aage, N., Niordson, C. F., & Sigmund, O. (2026). Mode I fracture toughness maximization of low-density architected materials. *International Journal of Solids and Structures*, 331, Article 113910. <https://doi.org/10.1016/j.ijsolstr.2026.113910>

General rights

Copyright and moral rights for the publications made accessible in the public portal are retained by the authors and/or other copyright owners and it is a condition of accessing publications that users recognise and abide by the legal requirements associated with these rights.

- Users may download and print one copy of any publication from the public portal for the purpose of private study or research.
- You may not further distribute the material or use it for any profit-making activity or commercial gain
- You may freely distribute the URL identifying the publication in the public portal

If you believe that this document breaches copyright please contact us providing details, and we will remove access to the work immediately and investigate your claim.



Contents lists available at ScienceDirect

International Journal of Solids and Structures

journal homepage: www.elsevier.com/locate/ijsolstr

Mode I fracture toughness maximization of low-density architected materials

Markus G. Holm¹*, Konstantinos Poulios¹, Niels Aage¹, Christian F. Niordson¹,
Ole Sigmund¹¹Department of Civil and Mechanical Engineering, Solid Mechanics, Technical University of Denmark, Nils Koppels Allé, B.404, Kgs. Lyngby, 2800, Hovedstaden, Denmark

ARTICLE INFO

Keywords:

Architected materials
Topology optimization
Lattice structures
Beam lattice microstructures
Fracture toughness

ABSTRACT

This paper presents a framework for systematically optimizing the fracture toughness of periodic beam lattice materials using topology optimization. We introduce a new normalization factor for fracture toughness based on the unit cell size arguing that it offers a more consistent and unambiguous basis for comparing different lattice microstructures than the conventional beam-length-based normalization. Our analysis demonstrates that the relative performance ranking of lattice topologies is significantly affected by the choice of normalization. Notably, when evaluated using this proposed unit-cell-based normalization, classical triangular and Kagome structures consistently demonstrate remarkably high fracture toughness, outperforming a demi-regular structure that appear superior under conventional beam-length normalization. This reinforces their established efficacy as high-performance lattice designs. The proposed optimization framework is applied to design lattice structures at low ($\bar{\rho} = 1\%$) and moderate ($\bar{\rho} = 15\%$) relative densities. Interestingly, the framework did not yield structures that surpassed the performance of the Kagome or triangular lattices when assessed with the proposed normalization factor. However, it is remarkable that when evaluated using the conventional beam-length-based normalization from the literature, the framework is able to generate a design that significantly outperforms the triangular and Kagome lattices, as well as a tension-dominated demi-regular structure, at moderate relative densities ($5\% < \bar{\rho} < 20\%$). This work highlights the critical influence of normalization choices on performance assessment and underscores the inherent efficiency of classical lattice topologies.

1. Introduction

Designing low-density materials with high structural resilience remains a fundamental challenge in solid mechanics. Conventional material systems often exhibit strong trade-offs between weight and mechanical performance, limiting their applicability in demanding engineering environments. Architected materials, and in particular periodic micro-lattice structures, provide a promising route to overcome these limitations by exploiting geometry to tailor stiffness, strength, and energy absorption. Despite these advantages, their practical implementation is constrained by a critical weakness: a pronounced susceptibility to damage and defects, which significantly reduces fracture resistance and compromises structural reliability. Addressing these limitations requires systematic approaches to enhance fracture toughness while preserving the lightweight characteristics that make these materials attractive.

Extensive work has been done to characterize the fracture toughness of lattice materials in 2D (Fleck and Qiu, 2007; Romijn and Fleck, 2007; Tankasala et al., 2015) and more recently in 3D (Shaikkea et al., 2022; Maurizi et al., 2022). Meanwhile, the literature is scarce

on systematic optimization of the fracture toughness of low-density lattice materials. A few studies, such as Lipperman et al. (2008, 2009), have explored parameter-based optimization of low-density lattice layouts using both beam-level and continuum descriptions. Furthermore, heuristic attempts to optimize the fracture toughness of lattice materials have been presented by Omidi and St-Pierre (2023a,b), where the authors suggest that demi-regular structures can outperform the classical triangular and Kagome structures. However, evaluation of the relative performance of these structures is obscured by the subjective choice of normalization parameters, which is discussed in the first section of this paper.

Several studies have investigated optimizing the fracture toughness of structures and porous materials using continuum topology optimization methods (Da and Qian, 2020; Jia et al., 2023; Gupta and Moini, 2024). These studies have shown that designs can be generated with exceptional fracture toughness, but they do not focus on periodic lattice materials specifically. Also, despite recent progress, explicit simulation of crack propagation remains computationally demanding, especially in

* Corresponding author.

E-mail address: mtaho@dtu.dk (M.G. Holm).<https://doi.org/10.1016/j.ijsolstr.2026.113910>

Received 2 October 2025; Received in revised form 27 January 2026; Accepted 14 February 2026

Available online 16 February 2026

0020-7683/© 2026 The Authors. Published by Elsevier Ltd. This is an open access article under the CC BY license (<http://creativecommons.org/licenses/by/4.0/>).

architected materials that require simulation of many cells to represent the periodic microstructure. Thus, the objective of this study is to optimize the microstructural layout of periodic beam lattice structures to enhance their resistance to brittle fracture, without explicitly simulating crack growth. This is achieved by focusing on optimizing the fracture toughness as a measure of the materials' ability to arrest cracks and prevent catastrophic failure.

2. Fracture toughness of lattice materials

In the context of Linear Elastic Fracture Mechanics (LEFM) the Mode I fracture toughness, K_{Ic} , is defined as the critical value of the stress intensity factor under Mode I loading, K_I . Following Fleck and Qiu (2007) this terminology can be applied to lattice materials, by assuming that crack growth initiates when the maximum local tensile stress at the outermost fiber of any lattice beam, σ_{max} , attains the tensile fracture stress, σ_f , of the solid.

In this study, the fracture toughness is investigated using a boundary layer model as detailed in Fleck and Qiu (2007). Here, a crack is introduced along the negative x_1 -direction and the K -displacement field for a homogeneous transversely isotropic continuum material is prescribed to the outer domain boundary C . The domain is discretized using a square finite element mesh composed of 96 by 96 unit cells similar to what is used in Fleck and Qiu (2007). This domain size was found sufficient to separate the scale of the asymptotic far-field and the near tip discreteness, as further increasing the domain size had negligible effect on the results. The maximum stress is obtained from a linear elastic quasi-static finite element analysis using Timoshenko beam elements with cubic interpolation functions (Cook et al., 2002) under plane strain conditions. The plane strain beam elements are chosen to represent long plate strips in the out-of-plane direction, and capture the deflection of a moderately thin plate with arbitrary end moments and shear forces. Thus, a single element for each beam is sufficient. For the presented numerical results, the constituent material is chosen as the Ti-6Al-4V alloy with the ultimate tensile strength of $\sigma_f = 600$ MPa similar to what is used in Tankasala et al. (2015).

It is important to note that for K to uniquely define the crack-tip stress conditions and be a valid fracture criterion, the cell size must be small compared to the singularity-dominated region governed by the K -field. Otherwise, the continuum assumption is invalid, and LEFM becomes inapplicable (Quintana-Alonso and Fleck, 2010). Hence, the application of LEFM for lattice materials can require domains spanning hundreds, or even thousands, of unit cells in each direction, particularly for the Kagome topology and other topologies that exhibit mechanism-like responses (Mane et al., 2024; Omid and St-Pierre, 2023a). Consequently, for many applications, the use of lattice materials falls outside the scope of LEFM and into the strength-based failure regime. In this strength regime, the performance rankings of different microstructures are highly dependent on the boundary conditions and must therefore be evaluated for each specific application. Thus, this work aims to investigate and optimize the fracture toughness of lattice materials within the LEFM framework, which provides a clear, well-established foundation for understanding fracture behavior in these materials, independent of boundary conditions.

However, a caveat in defining a lattice material's fracture toughness is its sensitivity to the pre-crack location within the unit cell, as discussed in Appendix A. While we observe some variation across different crack locations, the relative ranking of the microstructures remains unchanged, and the conclusions of this study are unaffected.

Another important assumption in this study is the evaluation of fracture toughness based on a single crack configuration. Since the objective of this study is to assess crack arrest and the prevention of catastrophic failure, fracture toughness is measured from the most favorable crack configuration, i.e., we hypothesize that the crack will inevitably have to pass through this state. Accordingly, we define

$$K_{Ic} = \max_{\alpha} K_{Ic}(\alpha) \quad (1)$$

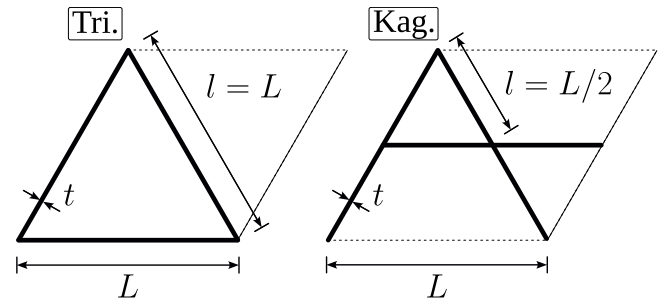


Fig. 1. Illustration of the unit cells for the triangular and Kagome microstructures, including the definition of the beam length, l , beam thickness, t , and unit cell size, L .

Table 1

Normalized fracture toughness for the structures shown in Fig. 2 for $\bar{\rho} = 15\%$.

	Tri.	Kag. ⁽⁻¹⁾	Kag.
$K_{Ic}/(\sigma_f\sqrt{l})$	0.091	-	0.120
$K_{Ic}/(\sigma_f\sqrt{L})$	0.091	0.079	0.088

where α denotes a discrete parameter representing different pre-crack positions relative to the microstructural layout. However, this definition is only meaningful if the crack configuration corresponding to $\max_{\alpha} K_{Ic}(\alpha)$ is actually realized during crack propagation. While this cannot be guaranteed for arbitrary architectures, it can be verified retrospectively by simulating crack propagation from multiple initial configurations and confirming that the maximum-toughness configuration occurs. Appendix B verifies that the maximum-toughness configuration indeed occurs in the lattice structures presented in the following subsection.

2.1. Comparing the fracture toughness of lattice structures

Among classical periodic microstructures, triangular and Kagome lattices are repeatedly reported to exhibit high fracture toughness (Fleck and Qiu, 2007; Omid and St-Pierre, 2023a). We therefore adopt these as reference structures and their unit cells are depicted in Fig. 1, with indication of the beam length l and unit-cell size L for each lattice.

Previous studies (Fleck and Qiu, 2007; Omid and St-Pierre, 2023a) suggests that the fracture toughness of a low-density linear elastic brittle lattice can be expressed using a simple power law relation:

$$K_{Ic} = D\bar{\rho}^d\sigma_f\sqrt{l} \quad (2)$$

where D and d are constants that depend on the topology of the microstructure. Thus, the fracture toughness scales with the square root of the beam length, \sqrt{l} , for a fixed relative density, $\bar{\rho}$. To explain this relation for the triangular microstructure, Fleck and Qiu (2007) present an analytical argument, which is summarized in the following paragraph.

The stresses ahead of the crack tip are approximated from the stress field immediately ahead of a Mode I crack in a continuum and are related to the applied Mode I stress intensity factor K_I by

$$\sigma_{11} = \sigma_{22} = \frac{K_I}{\sqrt{2\pi x_1}} \quad \text{and} \quad \sigma_{12} = 0 \quad (3)$$

where x_1 is the parallel distance from the crack tip. The average value of these stresses over one unit cell can be found by integrating the above stresses over one cell dimension and are thereby found to scale with \sqrt{l} . As these average stresses are assumed to be in equilibrium with the stresses within each beam in the unit cell, the maximum beam stress also scales with \sqrt{l} . Hence, increasing the unit cell size, L , and thereby the beam length, l , increases the performance by the

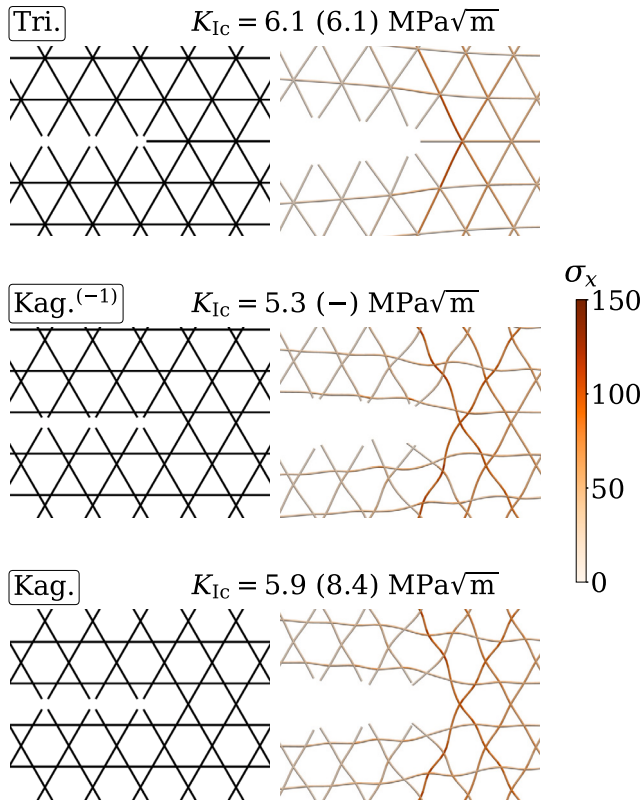


Fig. 2. Comparison of Mode I fracture toughness, K_{Ic} , for triangular (Tri.), intermediate Kagome (Kag.^(−1)), and Kagome (Kag.) microstructures. The results are shown for a relative density of $\bar{\rho} = 15\%$, a unit cell size of $L = 12.5$ mm, and a beam thickness of $t = 0.541$ mm, and $\sigma_f = 600$ MPa. The value in parentheses is the fracture toughness of the structure, scaled to maintain a fixed beam length of $l = 12.5$ mm.

square root of the size increase. This scaling argument by Fleck and Qiu (2007) could equivalently be formulated in terms of the unit cell size, L , and dimensional analysis supports the use of both \sqrt{l} and \sqrt{L} in Eq. (2). However, the choice of normalization factor has significant implications for the performance comparison between different microstructures, as discussed in the remainder of this section.

The size effect discussed above applies to all microstructure topologies, thus, the fracture toughness performance of different microstructures is often compared in the literature using the normalized measure $K_{Ic}/(\sigma_f\sqrt{l})$ (Fleck and Qiu, 2007; Omid and St-Pierre, 2023a). Comparing the performance using this normalized measure is equivalent to comparing structures with the same beam length l , and is therefore a design choice. Another design choice could be to compare structures with the same unit cell size or periodicity, L , which is equivalent to comparing structures using the normalized measure $K_{Ic}/(\sigma_f\sqrt{L})$. In the following, we examine the advantages and limitations of these two normalization approaches for comparing the fracture toughness across different microstructure topologies.

The normalization with \sqrt{l} has the key advantage of being directly related to the energy released when breaking a beam. However, it also has two drawbacks, which will be explained using an example based on the three microstructures shown in Fig. 2. This example is motivated by the fact that the triangular (Tri.) and Kagome (Kag.) microstructures have related unit cells, namely that the Kagome unit cell can be obtained by translating the horizontal beam of the triangular unit cell up to the center of the unit cell, as shown in Fig. 1. However, translating the lower beam of the triangular unit cell changes the

Table 2

Normalized fracture toughness for the structures shown in Fig. 3 for $\bar{\rho} = 15\%$.

	Kag. II	Kag. II opt
$K_{Ic}/(\sigma_f\sqrt{l})$	0.093	0.140
$K_{Ic}/(\sigma_f\sqrt{L})$	0.054	0.080

beam lengths, l , and it is clear that the individual beam lengths of the Kagome structure are now one half the unit cell size, L . Additionally, the middle microstructure in Fig. 2, denoted Kag.^(−1), is generated by translating the horizontal bar up by one-quarter of the unit cell height and can be seen as an intermediate Kagome structure. Furthermore, one could imagine generating numerous such intermediate structures by continuously translating the horizontal bar in the triangular unit cell.

The Kag.^(−1) microstructure has different beam lengths within the unit cell. Hence, it showcases the first drawback of the \sqrt{l} normalization; namely that it is unclear which beam length should be used for the normalization. The second drawback of the \sqrt{l} normalization is that it does not restrict the unit cell size. Thus, elaborate hierarchical lattices with large unit cells consisting of many short beams that effectively blunt the crack would be compared to, e.g., a triangular microstructure with a much smaller unit cell size.

Therefore, in the context of comparing the fracture toughness of different microstructure topologies, we instead propose the normalized measure $K_{Ic}/(\sigma_f\sqrt{L})$ where L is the unit cell size as shown in Fig. 1. Normalizing with \sqrt{L} allows comparison of microstructures with arbitrary beam lengths as it does not require definition of a fixed beam length within the microstructure.

Using this proposed normalization factor, an equivalent scaling law to Eq. (2) can be expressed with the unit cell size, L , replacing the beam length, l :

$$K_{Ic} = M\bar{\rho}^d\sigma_f\sqrt{L} \quad (4)$$

where M is a power law fitting parameter similar to D in Eq. (2). Note that for the triangular structure there is no difference between the power law parameters, meaning that $M = D$, while $M = D/\sqrt{2}$ for the Kagome structure.

Table 1 compares the performance for the structures shown in Fig. 2 using the two different normalization factors discussed above at a relative density of $\bar{\rho} = 15\%$. The results show that the Kagome microstructure significantly outperforms the triangular microstructure when normalizing with \sqrt{l} , whereas the triangular microstructure is superior when normalizing with \sqrt{L} . This is due to the $\sqrt{2}$ difference between the two measures for the Kagome structure. Essentially, normalizing with \sqrt{l} means that the triangular microstructure should be compared to a Kagome microstructure with twice the size of the unit cell, such that the structures have the same beam length l . In contrast, normalizing with \sqrt{L} means that the triangular and Kagome microstructures are compared for the same unit cell size, and the structures shown in Fig. 2 are therefore directly comparable.

To test the proposed normalization factor on more intricate microstructures, we apply it to the tension-dominated demi-regular structure investigated by Omid and St-Pierre (2023a), which we will denote Kag. II, and a structure obtained from the topology optimization framework presented in Section 3, which we will denote Kag. II opt. The two microstructures are shown in Fig. 3, where the beam thickness, t , has been adjusted for each structure to obtain a relative density of $\bar{\rho} = 15\%$ at the same unit cell size as the structures shown in Fig. 2.

The normalized fracture toughness of the structures shown in Fig. 3 are compared in Table 2. The results show that the Kag. II structure outperforms the triangular structure when using the \sqrt{l} normalization, which agrees with the results presented by Omid and St-Pierre (2023a). However, this is not the case when normalizing with \sqrt{L} .

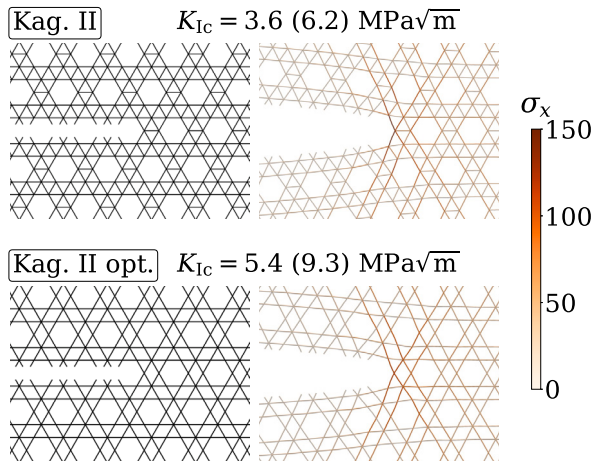


Fig. 3. Comparison of the Mode I fracture toughness, K_{Ic} , for the demi-regular double Kagome structure (Kag. II), and an optimized version of the double Kagome structure (Kag. II opt.). The results are shown for a relative density of $\bar{\rho} = 15\%$, unit cell size of $L = 12.5$ mm, $\sigma_f = 600$ MPa, and beam thickness of $t = 0.232$ mm and $t = 0.271$ mm for the Kag. II and Kag. II opt. structure, respectively. The value in parentheses is the fracture toughness of the structure, scaled to maintain a fixed beam length of $l = L = 12.5$ mm.

Furthermore, the Kag. II opt. microstructure significantly outperforms the triangular as well as all other Kagome microstructures when normalizing with \sqrt{l} , but not when normalizing with \sqrt{L} . The explanation is that these more intricate structures have significantly larger unit cells than beam lengths, specifically $L = 3l$ for both structures. Thus, when normalizing with the beam length, l , the performance is scaled by a factor of $\sqrt{3}$, which is not the case when normalizing with the unit cell size L .

To also compare the scaling of the critical toughness for the different structures, we employ the critical energy release rate, G_c , similar to [Omidi and St-Pierre \(2023b\)](#), which is found for pure Mode I in the assumed plane strain conditions as

$$G_c = (1 - \nu^2) \frac{K_{Ic}^2}{E} \quad (5)$$

The homogenized Young's modulus scaling law is defined by [Fleck and Qiu \(2007\)](#) as $E = B\bar{\rho}^b E_s$ in terms of the constituent Young's modulus, E_s , and another set of power law parameters, B and b . This scaling law matches perfectly with the simulated results. Thus, using Eq. (4) together with the Young's modulus scaling allows the normalized toughness to be written as

$$\frac{G_c E_s}{\sigma_f^2 L} = (1 - \nu^2) \frac{M^2}{B} \bar{\rho}^{2d-b} \quad (6)$$

The above normalized toughness measure is shown in [Table 3](#), together with the normalized stiffness, Poisson's ratio, and normalized fracture toughness to compare the five previously shown structures. The results indicate that the triangular structure outperforms the Kagome structure and all other structures in terms of fracture toughness and toughness for $\bar{\rho} > 6.5\%$ (4% with \sqrt{l} normalization).

Apart from the shifting of the curves due to the proposed \sqrt{L} normalization, the results presented here are in good agreement with results presented in previous studies ([Fleck and Qiu, 2007](#); [Romijn and Fleck, 2007](#); [Hsieh et al., 2020](#); [Omidi and St-Pierre, 2023a](#)). For example, the scaling factor for the triangular structure ranges in the literature between $0.500 \leq D \leq 0.607$. The spread in the values reported in the literature is likely due to the deviations from the simple power law relation at moderate and very low relative densities as seen in [Fig. 4a](#). This deviation is especially evident when observing the scaling of the normalized toughness measure in [Fig. 4b](#), which scales with K_{Ic}^2 .

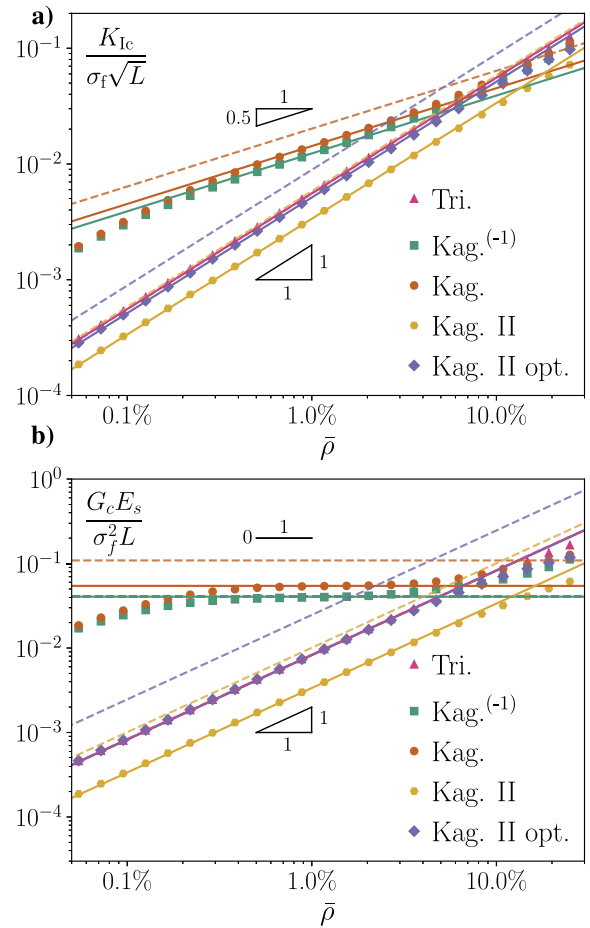


Fig. 4. Scaling of the normalized fracture toughness (a) and normalized toughness (b) for the structures shown in [Figs. 2 and 3](#). Solid lines represent power-law fits to the data, while dashed lines (shown with reduced opacity) correspond to analogous fits obtained using normalization with respect to the square root of the beam length, \sqrt{l} .

Table 3

Comparison of the normalized Young's modulus, Poisson's ratio, normalized fracture toughness, and normalized toughness for the five presented structures.

	E/E_s	ν	$\frac{K_{Ic}}{\sigma_f \sqrt{L}}$	$\frac{G_c E_s}{\sigma_f^2 L}$
Tri.	$0.333 \bar{\rho}$	0.333	$0.558 \bar{\rho}$	$0.830 \bar{\rho}$
Kag. ⁽⁻¹⁾	$0.333 \bar{\rho}$	0.333	$0.123 \sqrt{\bar{\rho}}$	0.0406
Kag.	$0.333 \bar{\rho}$	0.333	$0.143 \sqrt{\bar{\rho}}$	0.0544
Kag. II	$0.292 \bar{\rho}$	0.364	$0.336 \bar{\rho}$	$0.336 \bar{\rho}$
Kag. II opt.	$0.333 \bar{\rho}$	0.333	$0.514 \bar{\rho}$	$0.822 \bar{\rho}$

These fitting plots indicate that the simple power law relation is only a good approximation for relative densities in the range $0.5\% \lesssim \bar{\rho} \lesssim 5\%$. Consequently, the power-law parameters are sensitive to the choice of data points included in the regression. Interestingly, for the Kag. and Kag.⁽⁻¹⁾ structures, the slope in the log-log plot in [Fig. 4](#) transitions from $d = 0.5$ to $d = 1$ for very low relative densities ($\bar{\rho} \lesssim 0.1\%$). This indicates a shift in deformation behavior from bending-dominated to stretch-dominated. As bending contributions become negligible relative to axial forces for very low densities, where the beam model response starts to resemble a truss model response. For example, for the Kag. lattice at $\bar{\rho} = 0.01\%$, the ratio between axial and bending stresses, σ_a/σ_b , equals 14.2, whereas at $\bar{\rho} = 1\%$ it equals 0.85.

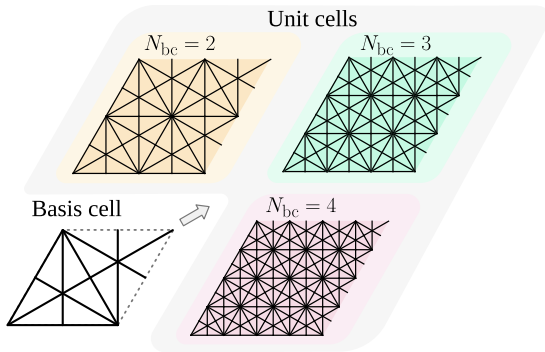


Fig. 5. Illustration of the chosen basis cell and its mapping to unit cells of increasing $N_{bc} \times N_{bc}$ number of basis cells.

3. Optimization

This study aims to maximize the fracture toughness of 2D periodic isotropic lattice materials by a topology optimization approach that introduces beam stiffnesses as design variables in a complex unit cell. The periodic isotropic lattice materials considered in this study offer reduced sensitivity to crack orientation due to their isotropy, and we hypothesize that the periodicity ensures that a crack will arrive at the most favorable crack arresting state as optimized for (and as verified in Appendix B). The periodic structures are generated by tessellating the unit cell design domain. Unit cells of different complexities are generated by mapping a basis cell as shown in Fig. 5, which shows that the generated unit cells contain $N_{bc} \times N_{bc}$ number of basis cells. This study is limited to the analysis of the basis cell with ground structure shown in Fig. 5, but remark that the presented method allows for exploration of more complicated basis cells as well. The topology of the basis cell is chosen such that it can represent the triangular and hexagonal structures for any N_{bc} , and the Kagome structure can be represented when N_{bc} is an even number.

Restricting the analysis to periodic lattices also enables the use of numerical homogenization, which allows constraints to be imposed on the constitutive matrix of the homogenized unit cell. The numerical homogenization follows the implementation presented by Vigliotti and Pasini (2012). This procedure gives an expression for the homogenized unit cell constitutive matrix, C^H , in the form

$$C^H = \frac{1}{S_{uc}} D_e^T K_{uc} D_e \quad (7)$$

where S_{uc} is the surface area of the unit cell, and D_e is a 3 column matrix found as the solution to the homogenization problem:

$$K_{uc} D_e^i = f(e^i), \quad \text{for } i = 1, 2, 3 \quad (8)$$

s.t. periodic BC's

where the superscript i refers to the i th column of D_e , and $f(e^i)$ is the right-hand-side vector corresponding to a prescribed unit strain of the i th in-plane strain component. Thus, each column of D_e represent the nodal displacements of the unit cell, corresponding to the unit strain, for each strain component. K_{uc} is the stiffness matrix of the unit cell, which is obtained using the standard finite element assembly procedure. Sensitivities of C^H with respect to design changes can be straightforwardly obtained as shown in Appendix D.2.

3.1. Optimization problem

The design variables are defined by the design variable vector $\mathbf{z} = \{x_t, \mathbf{x}\}^T$, which contains two types of design variables. Namely, a single design variable, x_t , to control the global beam thickness, $t(x_t)$, and a stiffness design variable vector, \mathbf{x} . The vector \mathbf{x} contains one design

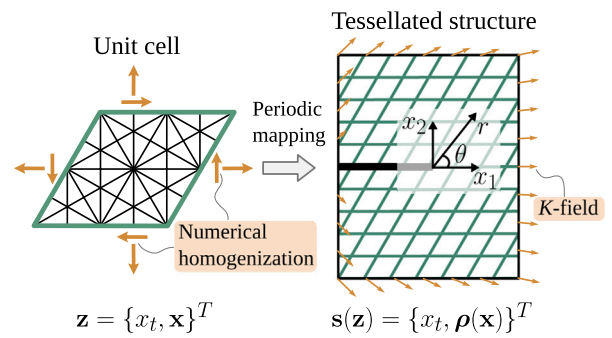


Fig. 6. Illustration of the design variables and boundary conditions associated with the unit cell and the tessellated structure, respectively.

variable per element in the unit cell controlling the artificial element density vector in the tessellated structure, $\rho(\mathbf{x})$, as illustrated in Fig. 6. To clarify the distinction between the unit cell design variables, \mathbf{z} , and the associated variables in the tessellated structure, we introduce the variable vector $\mathbf{s}(\mathbf{z}) = \{x_t, \rho(\mathbf{x})\}^T$ containing the design variables mapped to the tessellated structure.

The global beam thickness is interpolated linearly using x_t , and the stiffness of the e th element in the tessellated structure is interpolated using ρ_e according to the SIMP material model (Bendsoe, 1989; Sigmund, 2007):

$$t(x_t) = t_{\min} + x_t(t_{\max} - t_{\min}), \quad (9a)$$

$$\tilde{E}_e(\rho_e) = \frac{E_e(\rho_e)}{E_0} = \tilde{E}_{\min} + \rho_e^{q_k}(1 - \tilde{E}_{\min}) \quad (9b)$$

where $x_t, \rho_e \in [0, 1]$, and \tilde{E}_e is the dimensionless Young's modulus used to scale the stiffness matrix. To avoid premature convergence to local minima, we employ a relative low stiffness penalization factor of $q_k = 2$. Using the above parameterization, the global stiffness matrix $\mathbf{K}(\mathbf{s}(\mathbf{z}))$ is assembled from the element contributions as

$$\mathbf{K}(\mathbf{s}(\mathbf{z})) = \sum_{e=1}^{N_e} \tilde{E}_e(\rho_e) \mathbf{K}_e^0(t(x_t)) \quad (10)$$

where $\mathbf{K}_e^0(t(x_t))$ is the element stiffness matrix of a solid element ($x_e = 1$). The total volume of the unit cell per unit width, $V(\mathbf{z})$, is given by

$$V(\mathbf{z}) = \sum_{e=1}^{N_e} x_e t(x_t) l_e \quad (11)$$

where l_e is the strut length of the e th element.

In formulating the objective, it is noted that the fracture toughness can be written as

$$K_{Ic} = K_I \frac{\sigma_f}{\sigma_{\max}} = K_I \lambda \quad (12)$$

where $\lambda = \sigma_f/\sigma_{\max}$ is the load scaling factor. Thus, when prescribing a unit stress intensity factor, K_I , through the K -displacement field, the problem of maximizing K_{Ic} corresponds to maximizing λ or minimizing the maximum stress in the structure, σ_{\max} . Interestingly, the optimization process generates designs that are naturally aligned with their most favorable crack configuration, consistent with the definition in Section 2. However, a post-processing step is necessary to confirm that this configuration occurs during crack propagation, which is performed for the optimized structures in Appendix B.

Now we can formulate the optimization problem as

$$\min_{\mathbf{z}} \quad -\mathcal{J}(\mathbf{s}, \mathbf{u}(\mathbf{s})) = -\lambda(\mathbf{s}, \mathbf{u}(\mathbf{s})) + c M_{nd}(\mathbf{z}) \quad (13a)$$

$$\text{s.t.} \quad \mathbf{r}(\mathbf{s}) = \mathbf{K}(\mathbf{s})\mathbf{u}(\mathbf{s}) - \mathbf{f} = \mathbf{0}, \quad (13b)$$

$$g_{\text{vol}}(\mathbf{z}) = \bar{\rho}(\mathbf{z})/\bar{\rho}^* - 1 \leq 0, \quad (13c)$$

$$g_{\text{iso}}(C^H(\mathbf{z})) \leq 0, \quad (13d)$$

$$g_E(\mathbf{C}^H(\mathbf{z})) \leq 0, \quad (13e)$$

$$\mathbf{0} \leq \mathbf{z} \leq \mathbf{1} \quad (13f)$$

where $\mathbf{s} = \mathbf{s}(\mathbf{z})$ and the parameter $c = c_0 \lambda^{(0)}$ is used to control the amount of gray scale penalization, where $\lambda^{(0)}$ is the load scaling factor from the first iteration to ensure proper scaling. Further, $\bar{\rho}(\mathbf{z}) = V(\mathbf{z})/V_0$ is the physical relative density, $\bar{\rho}^*$ is the target physical relative density, and λ is the load scaling factor defined as

$$\lambda(\mathbf{s}, \mathbf{u}(\mathbf{s})) = \frac{\sigma_f}{\sigma_{\max}(\mathbf{s}, \mathbf{u}(\mathbf{s}))} \quad (14)$$

The variable $M_{\text{nd}}(\mathbf{z})$ is the measure of non-discreteness (Sigmund, 2007) defined as

$$M_{\text{nd}} = \frac{4}{N_e^{\text{uc}}} \sum_{e=1}^{N_e^{\text{uc}}} x_e(1 - x_e) \quad (15)$$

where N_e^{uc} is the number of elements in the unit cell. The term containing M_{nd} is included to penalize the use of intermediate densities, which has been found to be necessary to obtain a fully discrete design. The parameter c_0 is increased throughout the optimization, starting from zero during the first 200 iterations and increased using the sequence $c_0^{(n)} = \bar{c}_0 \gamma^{(n)}$ where n counts every 50th design iteration and the parameters are set to $\bar{c}_0 = 0.1$ and $\gamma = 1.5$ in the present study.

The constraints $g_{\text{vol}}(\mathbf{z})$ and $g_{\text{iso}}(\mathbf{C}^H(\mathbf{z}))$ are volume and isotropy constraints, respectively. The volume constraint is used to control the relative density of the structure, while the isotropy constraint is used to ensure that the constitutive matrix of the homogenized unit cell is elastically isotropic. The isotropy constraint is defined in Section 3.1.1. The constraint $g_E(\mathbf{C}^H(\mathbf{z}))$ is used to ensure that the homogenized unit cell Young's modulus, E is above some fraction of the Hashin-Shtrikman upper bound, and is defined in Section 3.1.2.

The optimization problem presented in Eq. (13) is solved using the method of moving asymptotes (MMA) (Svanberg, 1987).

The load scaling factor, λ , is computed using the stress-based fracture criterion presented in Section 2 and a p -norm approximation of the max function:

$$\lambda(\mathbf{s}) = \frac{\sigma_f}{\sigma_{\max}(\mathbf{s})} \quad (16)$$

$$\sigma_{\max}(\mathbf{s}) = \max(\boldsymbol{\sigma}(\mathbf{s})) \lesssim \sigma_{\text{PN}}(\mathbf{s}) \quad (17)$$

$$\sigma_{\text{PN}}(\mathbf{s}) = (\sigma_{\text{sum}}(\mathbf{s}))^{1/p} \quad (18)$$

$$\sigma_{\text{sum}}(\mathbf{s}) = \sum_{e=1}^{N_e} \sum_{n=1}^2 (\bar{\sigma}_e^n(\mathbf{s}))^p \quad (19)$$

where p is the p -norm parameter and $\bar{\sigma}_e^n$ is the relaxed stress measure of the e th element at node $n = \{1, 2\}$. Thus, the optimization problem is essentially a stress minimization problem around a pre-imposed crack subjected to the K -field boundary conditions as illustrated in Fig. 6. To avoid the influence of large stresses in low-density elements (the so-called stress singularity problem), stress relaxation is added to the element stress:

$$\bar{\sigma}_e^n(t(x_r)) = x_e^{q_\sigma} \sigma_e^n(t(x_r)) \quad (20)$$

where the stress measure of the e th element, σ_e^n , is selected as the maximum tensile stress within the e th element at node $n = \{1, 2\}$ computed as a solid element ($x_e = 1$). This stress is calculated as

$$\sigma_e^n = \max \left\{ 0, \frac{N_n^e}{A^e} + \frac{|M_n^e|}{W_b^e} \right\} \quad (21)$$

where A^e is the element area, W_b^e is the element section modulus, and N_n^e and M_n^e are the element section normal force and bending moment, respectively, found at the beam ends. The max operator is introduced to only account for tensile stresses, and the sensitivity of elements with negative stresses are thus zero. Note, all quantities in Eq. (21) depends explicitly on the beam thickness, $t(x_r)$, but the dependence is not written to ease the notation. The section forces at the beam ends

are equal to the internal forces at the nodes, which can be computed as

$$\begin{bmatrix} -N_1^e & -T_1^e & -M_1^e & N_2^e & T_2^e & M_2^e \end{bmatrix}^T = \mathbf{T}_e \mathbf{f}_{\text{int}}^e \quad (22)$$

where $\mathbf{T}_e = \mathbf{T}_e(\theta_e)$ is the transformation matrix that accounts for the orientation of the beam, $\mathbf{f}_{\text{int}}^e$ is the element internal force vector, and the signs are due to the sign convection used for computing stresses in beams. The element internal force vector is found as

$$\mathbf{f}_{\text{int}}^e = \mathbf{K}_e^0(t(x_r)) \mathbf{u}_e \quad (23)$$

The detailed adjoint sensitivity analysis of the objective function in Eq. (13) is presented in Appendix D.

3.1.1. Isotropy constraints on the homogenized unit cell constitutive matrix

The constitutive relations for a transversely isotropic elastic material can be written as

$$\mathbf{C}_{\text{iso}} = \begin{bmatrix} C_{11} & C_{12} & 0 \\ C_{12} & C_{11} & 0 \\ 0 & 0 & \frac{C_{11} - C_{12}}{2} \end{bmatrix}, \quad (24)$$

meaning that plane transversely isotropic materials satisfy the following relations

$$C_{11} - C_{22} = 0 \quad (25a)$$

$$\frac{(C_{11} - C_{12})}{2} - C_{33} = 0 \quad (25b)$$

$$C_{13} = 0 \quad (25c)$$

$$C_{23} = 0 \quad (25d)$$

Hence, to ensure that a unit cell remains transversely isotropic, the above relations can be introduced as constraints on the homogenized stiffness matrix of the unit cell, \mathbf{C}^H . Practically, the constraints are combined into a single constraint using a weighted sum and a tolerance factor of ϵ_{iso}

$$g_{\text{iso}}(\mathbf{C}^H(\mathbf{z})) = \frac{\sum_{i=1}^4 [\alpha_i g_{\text{iso},i}(\mathbf{z})^2]}{\epsilon_{\text{iso}}^2} - 1 \quad (26)$$

where $\sum_i \alpha_i = 1$ and the individual constraint functions, $g_{\text{iso},i}(\mathbf{z})$, are given as

$$g_{\text{iso},1} = \frac{C_{11}^H - C_{22}^H}{\frac{1}{2}(C_{11}^H + C_{22}^H)} \quad (27a)$$

$$g_{\text{iso},2} = \frac{C_{11}^H + C_{22}^H - 2(C_{12}^H + 2C_{33}^H)}{\frac{1}{2}(C_{11}^H + C_{22}^H)} \quad (27b)$$

$$g_{\text{iso},3} = \frac{C_{13}^H}{\frac{1}{2}(C_{11}^H + C_{22}^H)} \quad (27c)$$

$$g_{\text{iso},4} = \frac{C_{23}^H}{\frac{1}{2}(C_{11}^H + C_{22}^H)} \quad (27d)$$

where C_{11}^H has been replaced with $\bar{C}_{11}^H = \frac{1}{2}(C_{11}^H + C_{22}^H)$ and all constraints have been normalized with this mean value (Sigmund and Torquato, 1997). In the numerical implementation, the tolerance factor is set to $\epsilon_{\text{iso}} = 2.5\%$, and the weights are set to $\alpha_i = 0.25$.

3.1.2. Stiffness constraints on the homogenized stiffness matrix

To prevent the optimizer from converging to trivial solutions consisting with pure void ($x = 0$), which would exhibit negligible stresses and thus artificially high fracture toughness, we impose a minimum stiffness constraint on the homogenized unit cell. This ensures that the optimized design preserves a meaningful load-carrying capacity while improving fracture resistance. Thus, a constraint is added to enforce

that the structure retains a fraction, f_E , of the Hashin–Shtrikman (HS) upper bound on the effective Young’s modulus of a low-density ($\bar{\rho} \ll 1$) two-dimensional isotropic cellular solid, $E_{HS} = \frac{1}{3}E_s\bar{\rho}$. This constraint can be expressed as

$$E \geq f_E E_{HS} \quad (28)$$

The effective Young’s modulus of an isotropic periodic material can be computed from the homogenized constitutive matrix by solving

$$C_{11}^H = \frac{E}{1-\nu^2}, \quad C_{12}^H = \nu \frac{E}{1-\nu^2} \quad (29)$$

for E and ν , which gives

$$E = \frac{(C_{11}^H)^2 - (C_{12}^H)^2}{C_{11}^H}, \quad \nu = \frac{C_{12}^H}{C_{11}^H} \quad (30)$$

Inserting Eq. (30) into Eq. (28) gives the implemented constraint:

$$g_E(\mathbf{C}^H(\mathbf{z})) = 1 - \frac{\left(\frac{1}{2}(C_{11}^H + C_{22}^H) \right)^2 - (C_{12}^H)^2}{\left(\frac{1}{2}(C_{11}^H + C_{22}^H) \right)^2 f_E E_{HS}}$$

where, again, C_{11}^H is replaced with $\bar{C}_{11}^H = \frac{1}{2}(C_{11}^H + C_{22}^H)$.

4. Optimization results

To test the proposed optimization framework, we consider fracture toughness maximization of a periodic lattice material with a unit cell size of $L = 12.5$ mm and $N_{bc} = 4$ (Fig. 5). The optimization is performed for two different target relative densities, $\bar{\rho}^* = 1\%$ and $\bar{\rho}^* = 15\%$, as the relative difference in performance between structures is highly dependent on $\bar{\rho}$ as shown in Fig. 4. The results are generated using $p = 16$ for the p -norm approximation of the maximum stress, and the measure of non-discreteness penalty is applied after 200 iterations, but only if $M_{nd} > 1\%$ to avoid oscillations.

Running the optimization for a target relative density of $\bar{\rho}^* = 1\%$ results in the optimized structure being the classical Kagome structure, as shown in Fig. 7. The structure is generated from a uniform initial guess of the design variables, with a maximum beam thickness of $t_{max} = 0.067$ mm that allows for designing the largest possible Kagome structure within the unit cell, and requiring at least 50% of the Hashin–Shtrikman stiffness upper bound ($f_E = 0.5$). However, the stiffness constraint is only active in the initial phase of the optimization as the stiffness of the Kagome structure aligns with the Hashin–Shtrikman upper bound.

The design history shows a near monotonic decrease in the objective function, except minor oscillations as seen in Fig. 7a. The objective history also shows the load scaling factor evaluated using the true max function, which shows good agreement with the p -norm approximation but with slight oscillations. The first approximately 60 iterations are used to satisfy the stiffness constraint as shown in Fig. 7b. In satisfying the stiffness constraint, the global beam thickness is lowered due to the penalization of the intermediate artificial relative densities, ρ . Thus, it is beneficial to lower the global beam thickness to allow for more material to be available for increasing ρ . However, after finding an appropriate structure that satisfies the stiffness constraint, the global beam thickness is increased until the given structure utilizes all the volume with a near discrete solution.

It is not surprising that in this very low volume fraction regime ($\bar{\rho} = 1\%$), the optimized structure is the classical Kagome structure, which is recognized in the literature for having exceptional performance due to the $\sqrt{\bar{\rho}}$ scaling of the fracture toughness owing to the crack-tip blunting caused by the mechanism response near the crack tip (Fleck and Qiu, 2007). One of the aspirations of posing the optimization problem was to discover a new microstructure topology that could outperform the Kagome structure at low relative densities, but despite many experiments we have not identified such a microstructure.

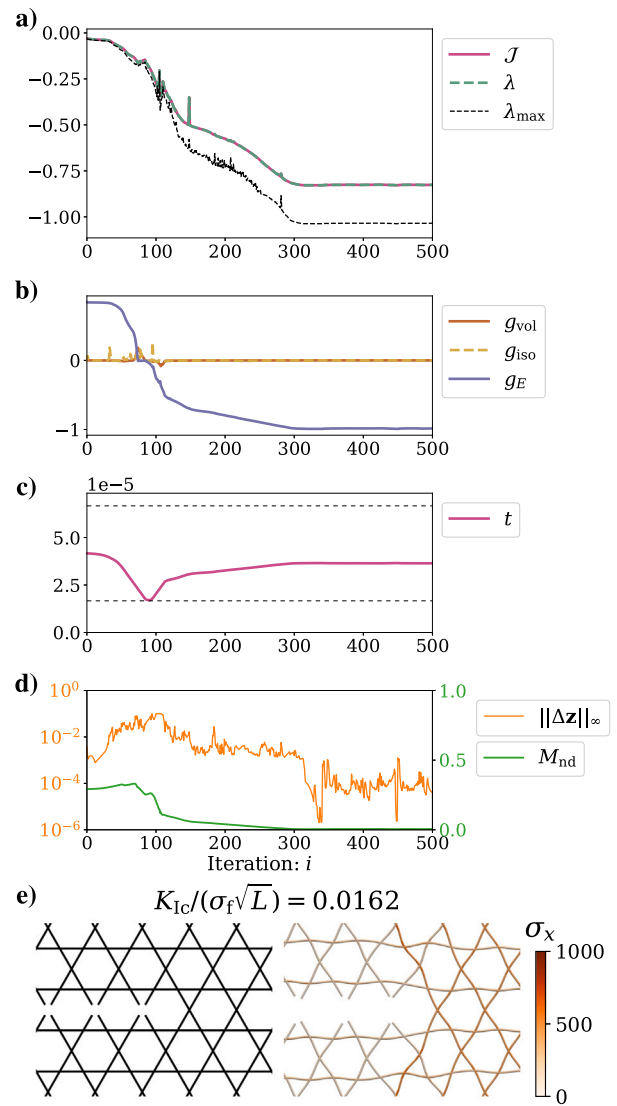


Fig. 7. (a) Design history of the objective, (b) constraints, (c) global beam thickness, (d) and changes in design variables and measure of non-discreteness. (e) shows the resulting optimized structure for a relative density of $\bar{\rho} = 1\%$, with a unit cell size of $L = 12.5$ mm. The structure is generated from a uniform initial guess of the design variables, $t_{max} = 0.067$ mm, $f_E = 0.5$, $N_{bc} = 4$, and the final beam thickness is $t = 0.036$ mm. For illustration purposes, the beam thickness has been visually scaled to 15 times the physical beam thickness.

To explain why the Kagome structure is difficult, if not impossible to beat, we present some additional optimization cases with a restriction of the maximum beam thickness, t_{max} and different initial guesses of the design variables. Note that restricting the maximum beam thickness forces the optimizer to utilize more elements in the unit cell, resulting in a more complex microstructure.

The first example is generated from an initial guess of the design variables where elements corresponding to the largest fitting triangular structure have a 10% larger value than the remaining gray elements, and we set $t_{max} = 0.020$ mm, and $f_E = 0.1$. This results in the optimized structure seen in Fig. 8a. The second example is generated from a uniform initial guess of the design variables, $t_{max} = 0.020$ mm and $f_E = 0.1$ and the optimized structure can be seen in Fig. 8b. Both structures are significantly more complex than the Kagome structure, but are poor constrained minima with respect to the fracture toughness as they have a significantly worse performance than the Kagome structure.

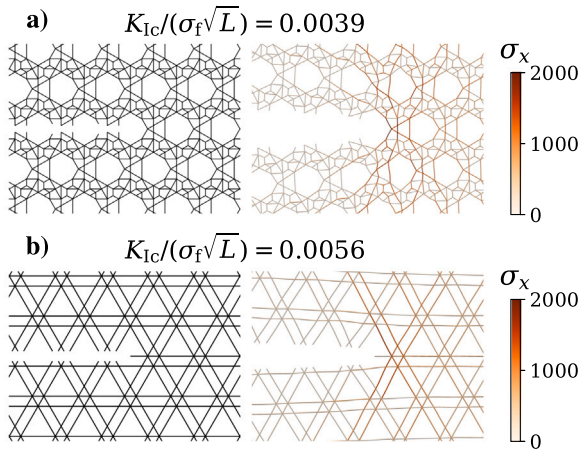


Fig. 8. Local minima optimized structures for a relative density of $\bar{\rho} = 1\%$, with a unit cell size of $L = 12.5$ mm. **(a)** is generated from an initial guess of the design variables where elements corresponding to the triangular structure has a 10% larger values than the remaining gray elements, $t_{\max} = 0.020$ mm, $N_{bc} = 4$, and $f_E = 0.1$, the final beam thickness is $t = 0.013$ mm. **(b)** is generated from a uniform initial guess, $f_E = 0.1$, $t_{\max} = 0.020$ mm, $N_{bc} = 4$ and the final beam thickness is $t = 0.018$ mm. For illustration purposes, the beam thickness has been scaled to 15 times the physical beam thickness due to the very low relative density.

One reason for the poor performance of these structures is that they are both tension dominated, which means that the performance scales approximately linearly with the relative density, $\bar{\rho}$, similar to the tension dominated structures shown in Fig. 4a. Another, more fundamental reason is that the complex structures get penalized by having shorter beam lengths, as discussed in Section 2. Thus, when comparing structures with the same unit cell size, L , as we propose in Section 2, it is beneficial to have a simple microstructure with long beams such as the Kagome or triangular structures.

The optimization is now repeated for a target relative density of $\bar{\rho}^* = 15\%$, which is a more moderate and realistic relative density where the tension dominated structures are expected to outperform the mechanism structures as shown in Fig. 4. The optimization is performed with a maximum beam thickness of $t_{\max} = 1.0$ mm, which allows for the design of both the largest fitting triangular and Kagome structures. The optimized structure is found to be the largest fitting triangular structure as shown in Fig. 9, which was also shown in Fig. 4 to be the best performing structure among the classical structures for moderate relative densities. This structure is best achieved from many different starting guesses. In particular, we used an initial guess of the design variables where elements corresponding to the triangular structure has a 10% larger initial value than the remaining gray elements, $t_{\max} = 1.0$ mm and $f_E = 0.5$.

Finally, the Kag. II. opt. structure presented in Section 2 is obtained by optimizing a slightly less complex unit-cell ground structure by setting $N_{bc} = 3$ and imposing a maximum beam thickness constraint of $t_{\max} = 0.300$ mm, which precludes configurations such as the largest admissible triangular structure. A uniform initial guess for the design variables is employed, and the stiffness constraint is enforced with $f_E = 0.5$. The optimized structure is shown in Fig. 10, and its performance is compared to existing designs in Section 2.

It is important to emphasize that under the \sqrt{l} normalization, corresponding to comparisons at a fixed beam length, the optimized structure in Fig. 10 exhibits a markedly superior performance relative to the best-performing configurations in the literature, including the triangular lattice, the Kagome lattice, and a tension-dominated demi-regular structure (Omid and St-Pierre, 2023a). In contrast, this

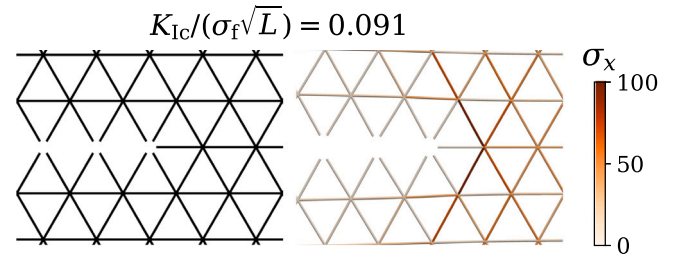


Fig. 9. Optimized structure for a relative density of $\bar{\rho} = 15\%$, with a unit cell size of $L = 12.5$ mm. The structure is generated from an initial guess of the design variables where elements corresponding to the triangular structure has 10% larger values than the remaining gray elements, $t_{\max} = 1.0$ mm, $f_E = 0.5$, $N_{bc} = 4$ and the final beam thickness is $t = 0.541$ mm. The illustrated beam thickness matches the physical beam thickness.

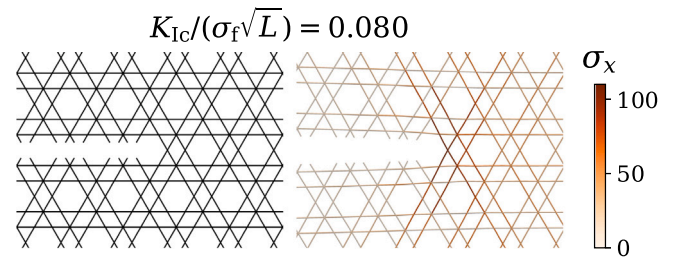


Fig. 10. Optimized structure for a relative density of $\bar{\rho} = 15\%$, with a unit cell size of $L = 12.5$ mm. The structure is generated from a uniform initial guess of the design variables with $t_{\max} = 0.300$ mm, $f_E = 0.5$, $N_{bc} = 3$ and the final beam thickness is $t = 0.271$ mm. The illustrated beam thickness matches the physical beam thickness.

advantage does not persist when employing the proposed \sqrt{L} normalization, which underlines the importance of consistent choices in performance evaluation.

5. Conclusions

This paper presents a framework for systematically optimizing the Mode I fracture toughness of periodic lattice materials using topology optimization. Another key contribution is the introduction of a normalization factor based on unit cell size rather than beam length. This eliminates ambiguity in beam-length definitions and reflects the approximate square-root scaling of fracture toughness with unit cell size, enabling fairer comparisons across microstructures.

Using this normalization, we demonstrate that a demi-regular structure, previously reported to outperform classical designs, does not surpass the triangular or Kagome lattices, contrary to conclusions drawn under beam-length-based normalization. The optimization framework was applied at low ($\bar{\rho} = 1\%$) and moderate ($\bar{\rho} = 15\%$) relative densities. At both densities, the optimized designs did not exceed the performance of the classical structures. Namely, the Kagome structure at low density and the triangular structure at moderate density, reinforcing the exceptional efficiency of these classical topologies.

It is however remarkable that, the designs produced by the proposed optimization framework, when evaluated using the conventional beam-length-based normalization, achieved substantially higher fracture toughness than the best-performing configurations in the literature for moderate relative densities ($5\% < \bar{\rho} < 20\%$). This finding underscores the critical influence of the choice of normalization when assessing the performance of different lattice topologies.

Table A.4

Comparison of the predicted K_{Ic} (MPa \sqrt{m}) obtained using the two different pre-crack modeling approaches: splitting nodes (Figs. 2 and 3) and splitting elements (Fig. A.11).

Pre-crack	Tri.	Kag. ⁽⁻¹⁾	Kag.	Kag. II	Kag. II opt.
Node-split	6.1	5.3	5.9	3.6	5.4
Element-split	5.9	5.5	5.9	3.6	5.4

CRedit authorship contribution statement

Markus G. Holm: Writing – review & editing, Writing – original draft, Visualization, Validation, Software, Methodology, Investigation, Formal analysis. **Konstantinos Poullos:** Writing – review & editing, Supervision, Methodology. **Niels Aage:** Writing – review & editing, Supervision, Methodology. **Christian F. Niordson:** Writing – review & editing, Supervision, Methodology. **Ole Sigmund:** Writing – review & editing, Supervision, Project administration, Methodology, Funding acquisition, Formal analysis, Conceptualization.

Replication of results

The results presented in this manuscript are reproducible through the implementation of the methodology described. The numerical setup, including all parameters and boundary conditions, is detailed in the paper. Readers interested in replicating the results may contact the corresponding author for further clarification or access to supplementary details.

Declaration of competing interest

The authors declare that they have no known competing financial interests or personal relationships that could have appeared to influence the work reported in this paper.

Acknowledgments

This research is supported by the Villum Foundation, Denmark, as part of the Villum Investigator Project “AMSTRAD” (VIL54487).

Appendix A. Influence of the pre-crack location

This appendix investigates the influence of the pre-crack location on both the classical and optimized microstructures. In the main text, the pre-crack is introduced by removing all elements along the vertical centerline of the unit cell as illustrated in Figs. 2 and 3. This is similar to the approach widely used in the literature (Fleck and Qiu, 2007; Tankasala et al., 2015; Omid and St-Pierre, 2023a), where the nodes are split across the cracking plane. While this facilitates comparison with existing results, it is important to investigate whether the chosen pre-crack location affects the relative performance of the different structures. To this end, we also consider an alternative pre-crack configuration where elements are removed along a horizontal line placed slightly above the nodes. This more closely resembles the true location of a long propagating crack (Lipperman et al., 2007).

The alternative pre-crack configuration is illustrated in Fig. A.11. Although this approach produces a small shift in the predicted fracture toughness (Table A.4), the relative ranking of the structures remains unchanged, especially when considered across different relative densities. Thus, the conclusions reported in the main text regarding the relative performance of the microstructures are robust to the choice of pre-crack definition.

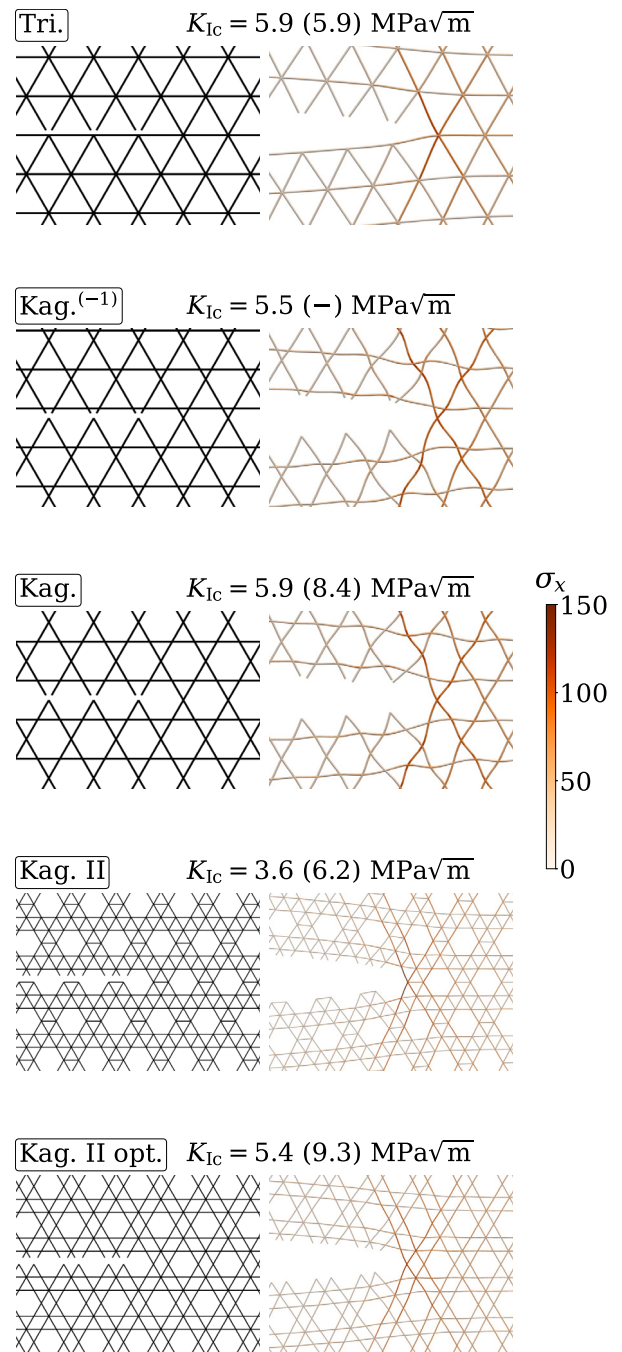


Fig. A.11. Comparison of the Mode I fracture toughness, K_{Ic} , using an alternative pre-crack method for the structures in Figs. 2 and 3, with all other simulation parameters kept constant. The value in parentheses is the fracture toughness of the structure, scaled to maintain a fixed beam length of $l = L = 12.5$ mm.

Appendix B. Verification of the maximum fracture toughness crack configuration

As discussed in Section 2, a key assumption of this work is the definition of the fracture toughness associated with the most favorable crack configuration, based on the hypothesis that a propagating crack will inevitably pass through this configuration. This hypothesis is verified retrospectively for the existing and optimized structures presented

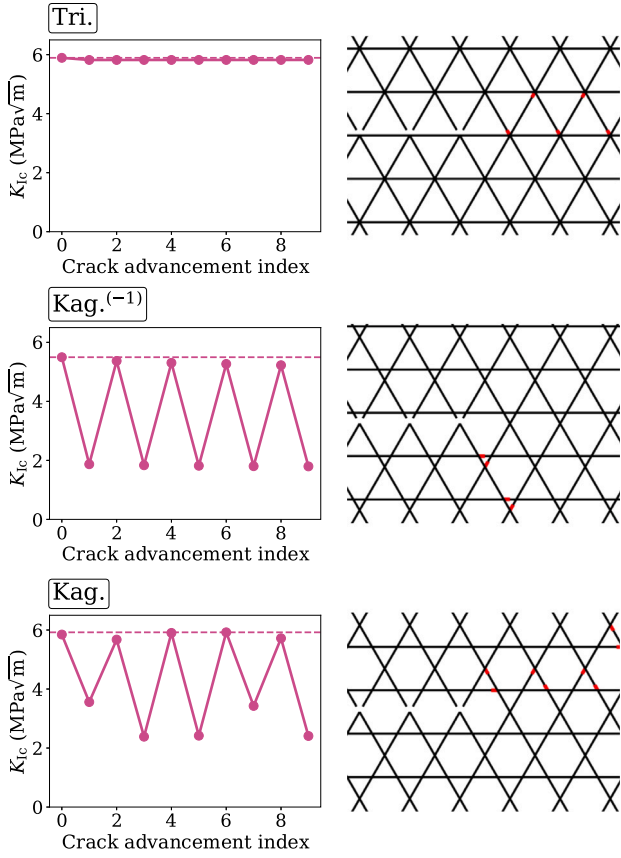


Fig. B.12. Crack propagation study for the structures in Fig. 2.

in Section 2 by simulating crack growth from multiple initial configurations and confirming that the maximum-toughness configuration arises.

For the simple lattice structures shown in Fig. 2, a single initial crack configuration combined with a few propagation simulations suffices to verify the occurrence of the maximum-toughness configuration, as demonstrated in Fig. B.12. The triangular lattice exhibits a constant fracture toughness due to its symmetry and straightforward crack path. The simple Kagome-type structures alternate between a weak and strong crack configuration, with the strong configuration remaining remarkably consistent even when the crack kinks. The minor variations observed in K_{Ic} for identical crack configurations arise from finite-boundary effects in the simulations and could be eliminated by enlarging the domain, but are insignificant for the purposes of this analysis.

The more complex microstructures illustrated in Fig. 3 require two distinct initial crack positions to verify that the maximum-toughness configuration is realized during crack propagation, as shown in Fig. B.13. The results confirm that the maximum-toughness configuration is indeed reached for these structures as well. Consequently, this validates the fracture-toughness definition adopted in this work for all considered microstructures, except for the poorly constrained minima shown in Fig. 8.

Appendix C. K -displacement field for mode I

The Mode I K -displacement field for a homogeneous and isotropic solid can be written as (Fleck and Qiu, 2007):

$$u_1 = \frac{K_I}{2\sqrt{2\pi G}} r^{1/2} (\kappa - \cos \theta) \cos \frac{\theta}{2} \quad (C.1)$$

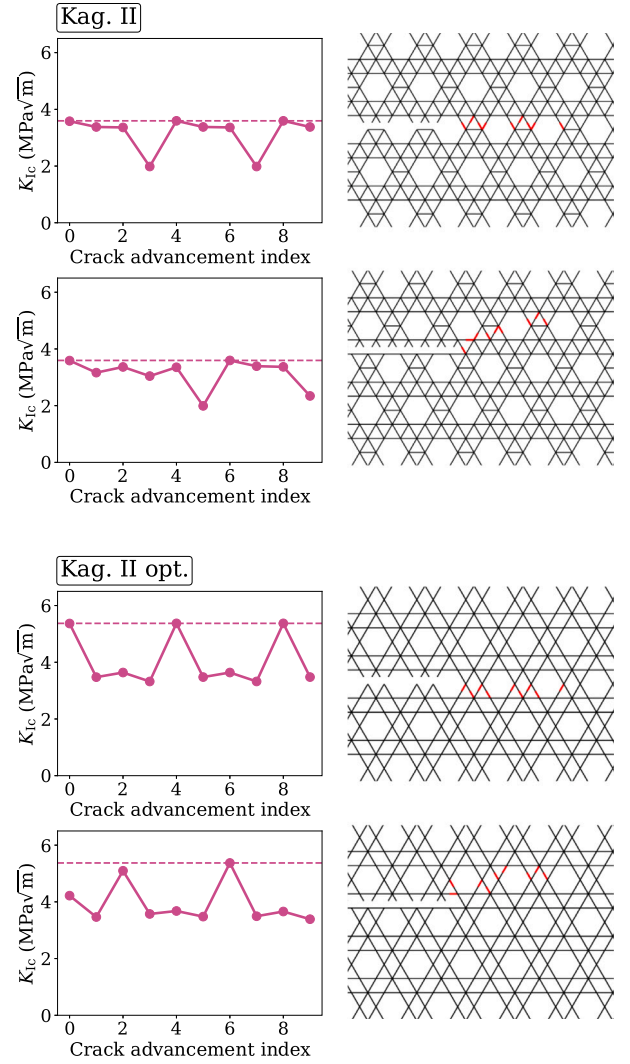


Fig. B.13. Crack propagation study for the structures in Fig. 3.

$$u_2 = \frac{K_I}{2\sqrt{2\pi G}} r^{1/2} (\kappa - \cos \theta) \sin \frac{\theta}{2} \quad (C.2)$$

$$\omega = -\frac{1 + \kappa}{4\sqrt{2\pi}} \frac{K_I}{G} r^{-1/2} \sin \frac{\theta}{2} \quad (C.3)$$

where u_1, u_2 and ω are nodal displacements and rotations, respectively, r and θ are the polar coordinates from the crack tip as shown in Fig. 6. Further, $G = E/(2(1 + \nu))$ is the homogenized shear modulus, and $\kappa = (3 - \nu_{ps})/(1 + \nu_{ps})$. For the assumed transversely isotropic material, the plane strain Poisson ratio can be computed as

$$\nu_{ps} = \frac{\nu + \gamma}{1 - \gamma}, \quad \gamma = \frac{E\nu_s^2}{\bar{\rho}E_s} \quad (C.4)$$

where ν_s and E_s are the Poisson ratio and Young's modulus of the constituent material, respectively, and $\bar{\rho}$ is the relative density of the lattice material.

Beam elements are used to approximate long plate strips, meaning that the material properties of the beam elements are defined as

$$E_s^{\text{beam}} = \frac{E_s}{1 - \nu_s^2} \quad \text{and} \quad \nu_s^{\text{beam}} = \frac{\nu_s}{1 - \nu_s} \quad (C.5)$$

Appendix D. Sensitivity analysis

D.1. Adjoint sensitivity analysis of the objective function

We employ adjoint sensitivity analysis to find the sensitivity of the load scaling factor with respect to the design variables \mathbf{z} . This is equivalent to solving a subproblem on the form:

$$\min_{\mathbf{z}} -\lambda(\mathbf{s}, \mathbf{u}(\mathbf{x})) \quad (\text{D.1a})$$

$$\text{s.t. } \mathbf{r}(\mathbf{x}, \mathbf{u}(\mathbf{x})) = \mathbf{0} \quad (\text{D.1b})$$

where $\mathbf{s} = \mathbf{s}(\mathbf{z})$ as shown in Fig. 6. It is clear that the K -field boundary conditions depends on the homogenized constitutive properties and thereby on the design vector, \mathbf{z} , i.e. $G = G(\mathbf{C}^H(\mathbf{z}))$ and $\kappa = \kappa(\mathbf{C}^H(\mathbf{z}))$. Thus, the K -field boundary conditions constitute design-dependent loads. Using that the boundary conditions are imposed as Dirichlet conditions, the global displacement vector is decomposed as

$$\mathbf{u}(\mathbf{s}, \mathbf{z}) = \mathbf{B}_f \mathbf{u}_f(\mathbf{s}) + \mathbf{B}_p \mathbf{u}_p(\mathbf{s}) \quad (\text{D.2})$$

where \mathbf{B}_f and \mathbf{B}_p are non-square indicator matrices that map the *free* and *prescribed* DoFs to the global system, respectively. Likewise, \mathbf{u}_f and \mathbf{u}_p are the displacement vectors associated with the *free* and *prescribed* DoFs, respectively. Hence, the residual equilibrium equations for the *free* system without external force loads ($\mathbf{f} = \mathbf{0}$) can be written as

$$\mathbf{r}_f = \mathbf{B}_f^T \mathbf{K} \mathbf{u} = \mathbf{B}_f^T \mathbf{K}(\mathbf{s}) \left[\mathbf{B}_f \mathbf{u}_f(\mathbf{s}) + \mathbf{B}_p \mathbf{u}_p(\mathbf{s}) \right] = \mathbf{0} \quad (\text{D.3})$$

where $\mathbf{r}_f = \mathbf{r}_f(\mathbf{s}, \mathbf{u}(\mathbf{s}))$, and we obtain the negative Lagrangian of the stress subproblem (Eq. (D.1)) as

$$-\mathcal{L}_\sigma(\mathbf{s}(\mathbf{z}), \mathbf{u}(\mathbf{s}(\mathbf{z}))) = \lambda(\mathbf{s}, \mathbf{u}(\mathbf{s})) - \Lambda_f^T \mathbf{r}_f(\mathbf{s}, \mathbf{u}(\mathbf{s})) \quad (\text{D.4})$$

Thus, the derivative of the Lagrangian with respect to the i th design variable, z_i , is found as

$$\begin{aligned} \frac{\partial \mathcal{L}_\sigma}{\partial z_i} &= \frac{\partial \lambda}{\partial \mathbf{s}} \frac{\partial \mathbf{s}}{\partial z_i} + \frac{\partial \lambda}{\partial \mathbf{u}} \left[\mathbf{B}_f \frac{\partial \mathbf{u}_f}{\partial \mathbf{s}} \frac{\partial \mathbf{s}}{\partial z_i} + \mathbf{B}_p \frac{\partial \mathbf{u}_p}{\partial z_i} \right] - \\ &\Lambda_f^T \mathbf{B}_f^T \left[\frac{\partial \mathbf{K}}{\partial \mathbf{s}} \frac{\partial \mathbf{s}}{\partial z_i} \mathbf{u} + \mathbf{K} \mathbf{B}_f \frac{\partial \mathbf{u}_f}{\partial \mathbf{s}} \frac{\partial \mathbf{s}}{\partial z_i} + \mathbf{K} \mathbf{B}_p \frac{\partial \mathbf{u}_p}{\partial z_i} \right] \end{aligned}$$

and we collect terms with the derivatives $\partial \mathbf{u}_f / \partial \mathbf{s}$ that cannot be directly determined as

$$\begin{aligned} \frac{\partial \mathcal{L}_\sigma}{\partial z_i} &= \frac{\partial \lambda}{\partial \mathbf{s}} \frac{\partial \mathbf{s}}{\partial z_i} + \frac{\partial \lambda}{\partial \mathbf{u}} \mathbf{B}_p \frac{\partial \mathbf{u}_p}{\partial z_i} - \Lambda_f^T \mathbf{B}_f^T \left[\frac{\partial \mathbf{K}}{\partial \mathbf{s}} \frac{\partial \mathbf{s}}{\partial z_i} \mathbf{u} + \mathbf{K} \mathbf{B}_p \frac{\partial \mathbf{u}_p}{\partial z_i} \right] + \\ &\underbrace{\left[\frac{\partial \lambda}{\partial \mathbf{u}} \mathbf{B}_f - \Lambda_f^T \mathbf{B}_f^T \mathbf{K} \mathbf{B}_f \right]}_{=0 \text{ (Eq. (D.6))}} \frac{\partial \mathbf{u}_f}{\partial \mathbf{s}} \frac{\partial \mathbf{s}}{\partial z_i} \end{aligned} \quad (\text{D.5})$$

where the adjoint problem is identified as

$$\frac{\partial \lambda}{\partial \mathbf{u}} \mathbf{B}_f - \Lambda_f^T \mathbf{B}_f^T \mathbf{K} \mathbf{B}_f = \mathbf{0} \quad (\text{D.6})$$

The above Eq. (D.6) is equivalent to solving for the adjoint vector only in the *free* DoFs of the system and setting the remaining adjoint vector values associated with the prescribed DoFs to zero:

$$\mathbf{K}_{ff} \Lambda_f = \mathbf{B}_f^T \left(\frac{\partial \lambda}{\partial \mathbf{u}} \right)^T, \quad \Lambda_p = \mathbf{0} \quad (\text{D.7})$$

where the stiffness matrix of the *free* system is defined as $\mathbf{K}_{ff} = \mathbf{B}_f^T \mathbf{K} \mathbf{B}_f$, which has already been factorized for solving the state problem. Having solved the adjoint problem, the sensitivities can be determined using Eq. (D.5):

$$\frac{\partial \mathcal{L}_\sigma}{\partial z_i} = \frac{\partial \lambda}{\partial \mathbf{s}} \frac{\partial \mathbf{s}}{\partial z_i} + \frac{\partial \lambda}{\partial \mathbf{u}} \mathbf{B}_p \frac{\partial \mathbf{u}_p}{\partial z_i} - \Lambda_f^T \mathbf{B}_f^T \left[\frac{\partial \mathbf{K}}{\partial \mathbf{s}} \frac{\partial \mathbf{s}}{\partial z_i} \mathbf{u} + \mathbf{K} \mathbf{B}_p \frac{\partial \mathbf{u}_p}{\partial z_i} \right] \quad (\text{D.8})$$

Hence, obtaining the sensitivities requires the derivatives $\partial \lambda / \partial x_i$, $\partial \lambda / \partial \rho_e$, $\partial \lambda / \partial \mathbf{u}$, and $\partial \mathbf{u}_p / \partial z_i$ which will be derived in the following.

Note, the derivative $\partial \mathbf{s} / \partial z_i$, essentially sums the contributions from each element in the tessellated structure to the corresponding element in the unit cell.

Adding the sensitivities of the measure of non-discreteness to the sensitivities of the stress subproblem (Eq. (D.8)) gives the sensitivity of the Lagrangian for the full objective function (Eq. (13)):

$$-\frac{\partial \mathcal{L}}{\partial z_i} = -\frac{\partial \mathcal{L}_\sigma}{\partial z_i} + c_{G_x} \lambda^{(0)} \frac{\partial M_{nd}(\mathbf{x})}{\partial \mathbf{x}} \quad (\text{D.9})$$

where

$$\frac{\partial M_{nd}(\mathbf{x})}{\partial x_e} = \frac{4}{N_e^{\text{uc}}} (1 - 2x_e) \quad (\text{D.10})$$

The partial derivative $\partial \lambda / \partial \rho_e$ can be obtained as:

$$\frac{\partial \lambda}{\partial \rho_e} = -\frac{\sigma_c}{\sigma_{\max}^2} \frac{\partial \sigma_{\max}}{\partial \rho_e} \quad (\text{D.11})$$

$$\frac{\partial \sigma_{\max}}{\partial \rho_e} = \frac{1}{p} (\sigma_{\text{sum}})^{\frac{1}{p}-1} \frac{\partial \sigma_{\text{sum}}}{\partial \rho_e} \quad (\text{D.12})$$

$$\frac{\partial \sigma_{\text{sum}}}{\partial \rho_e} = \sum_{n=1}^2 p (\bar{\sigma}_e^n)^{p-1} \frac{\partial \bar{\sigma}_e^n}{\partial \rho_e} \quad (\text{D.13})$$

$$\frac{\partial \bar{\sigma}_e^n}{\partial \rho_e} = q_\sigma \rho_e^{q_\sigma-1} \sigma_e^n \quad (\text{D.14})$$

The partial derivative $\partial \lambda / \partial x_i$ can be obtained as:

$$\frac{\partial \lambda}{\partial x_i} = -\frac{\sigma_c}{\sigma_{\max}^2} \frac{\partial \sigma_{\max}}{\partial x_i} \quad (\text{D.15a})$$

$$\frac{\partial \sigma_{\max}}{\partial x_i} = \frac{1}{p} (\sigma_{\text{sum}})^{\frac{1}{p}-1} \frac{\partial \sigma_{\text{sum}}}{\partial x_i} \quad (\text{D.15b})$$

$$\frac{\partial \sigma_{\text{sum}}}{\partial x_i} = \sum_{n=1}^2 p (\bar{\sigma}_e^n)^{p-1} \frac{\partial \bar{\sigma}_e^n}{\partial x_i} \quad (\text{D.15c})$$

$$\frac{\partial \bar{\sigma}_e^n}{\partial x_i} = \rho_e^{q_\sigma} \frac{\partial \sigma_e^n}{\partial x_i} \quad (\text{D.15d})$$

$$\frac{\partial \sigma_e^n}{\partial x_i} = \frac{\partial N_n^e}{\partial x_i} \frac{1}{A_e} - \frac{N_n^e}{(A_e)^2} \frac{\partial A_e}{\partial x_i} + \quad (\text{D.15e})$$

$$\frac{M_n^e}{|M_n^e|} \frac{\partial M_n^e}{\partial x_i} \frac{1}{W_b^e} - \frac{|M_n^e|}{(W_b^e)^2} \frac{\partial W_b^e}{\partial x_i}$$

The derivatives of the section forces are proportional to the derivatives of the internal forces and can be found as

$$\left[-\frac{\partial N_1^e}{\partial x_i} \quad -\frac{\partial T_1^e}{\partial x_i} \quad -\frac{\partial M_1^e}{\partial x_i} \quad \frac{\partial N_2^e}{\partial x_i} \quad \frac{\partial T_2^e}{\partial x_i} \quad \frac{\partial M_2^e}{\partial x_i} \right]^T = \mathbf{T}_e \frac{\partial \mathbf{f}_{\text{int}}^e}{\partial x_i}$$

where

$$\frac{\partial \mathbf{f}_{\text{int}}^e}{\partial x_i} = \frac{\partial \mathbf{K}_e^0(t(x_i))}{\partial x_i} \mathbf{u}_e \quad (\text{D.16})$$

The partial derivative $\partial \lambda / \partial \mathbf{u}$ is obtained by finite element assembly of the element-wise partial derivatives, $\partial \lambda / \partial \mathbf{u}_e$:

$$\frac{\partial \lambda}{\partial \mathbf{u}_e} = -\frac{\sigma_c}{\sigma_{\max}^2} \frac{\partial \sigma_{\max}}{\partial \mathbf{u}_e} \quad (\text{D.17a})$$

$$\frac{\partial \sigma_{\max}}{\partial \mathbf{u}_e} = c \frac{1}{p} (\sigma_{\text{sum}})^{\frac{1}{p}-1} \frac{\partial \sigma_{\text{sum}}}{\partial \mathbf{u}_e} \quad (\text{D.17b})$$

$$\frac{\partial \sigma_{\text{sum}}}{\partial \mathbf{u}_e} = \sum_{n=1}^2 p (\bar{\sigma}_e^n)^{p-1} \frac{\partial \bar{\sigma}_e^n}{\partial \mathbf{u}_e} \quad (\text{D.17c})$$

$$\frac{\partial \bar{\sigma}_e^n}{\partial \mathbf{u}_e} = \rho_e^{q_\sigma} \frac{\partial \sigma_e^n}{\partial \mathbf{u}_e} \quad (\text{D.17d})$$

$$\frac{\partial \sigma_e^n}{\partial \mathbf{u}_e} = \frac{\partial N_n^e}{\partial \mathbf{u}_e} \frac{1}{A_e} + \frac{M_n^e}{|M_n^e|} \frac{\partial M_n^e}{\partial \mathbf{u}_e} \frac{1}{W_b^e} \quad (\text{D.17e})$$

where the partial derivatives of the bending moments are found as

$$\left[-\frac{\partial N_1^e}{\partial \mathbf{u}_e} \quad -\frac{\partial T_1^e}{\partial \mathbf{u}_e} \quad -\frac{\partial M_1^e}{\partial \mathbf{u}_e} \quad \frac{\partial N_2^e}{\partial \mathbf{u}_e} \quad \frac{\partial T_2^e}{\partial \mathbf{u}_e} \quad \frac{\partial M_2^e}{\partial \mathbf{u}_e} \right]^T = \mathbf{T}_e \frac{\partial \mathbf{f}_{\text{int}}^e}{\partial \mathbf{u}_e}$$

where

$$\frac{\partial \mathbf{f}_{\text{int}}^e}{\partial \mathbf{u}_e} = \mathbf{K}_e^0(t(x_i)) \quad (\text{D.18})$$

We find the individual components of $\partial \mathbf{u}_p / \partial z_i$ from the K -field as

$$\frac{\partial u_1}{\partial z_i} = \frac{K_1 r^{1/2} \cos \frac{\theta}{2}}{2\sqrt{2\pi}} \left[\frac{\kappa' G - (\kappa - \cos(\theta))G'}{G^2} \right]$$

$$\frac{\partial u_2}{\partial z_i} = \frac{K_1 r^{1/2} \sin \frac{\theta}{2}}{2\sqrt{2\pi}} \left[\frac{\kappa' G - (\kappa - \cos(\theta))G'}{G^2} \right]$$

$$\frac{\partial \omega}{\partial z_i} = -\frac{K_1 r^{-1/2} \sin \frac{\theta}{2}}{4\sqrt{2\pi}} \left[\frac{\kappa' G - (1 + \kappa)G'}{G^2} \right]$$

where $\square' = \partial \square / \partial z_i$, $\kappa = \kappa(z_i)$ and $G = G(z_i)$.

Finally, for completeness, we present the additional derivatives as

$$\frac{\partial G}{\partial z_i} = \frac{E'(1 + \nu) - E\nu'}{2(1 + \nu)^2} \quad (\text{D.20a})$$

$$\frac{\partial \kappa}{\partial z_i} = -\frac{4\nu'_{\text{ps}}}{(1 + \nu_{\text{ps}})^2} \quad (\text{D.20b})$$

$$\frac{\partial \nu_{\text{ps}}}{\partial z_i} = \frac{(1 - \gamma)\nu' + (1 + \nu)\gamma'}{(1 - \gamma)^2} \quad (\text{D.20c})$$

$$\frac{\partial \gamma}{\partial z_i} = \frac{\nu_s^2 E' \bar{\rho} - E \bar{\rho}'}{E_s \bar{\rho}^2} \quad (\text{D.20d})$$

$$\frac{\partial E}{\partial z_i} = \frac{\left((\bar{C}_{11}^{\text{H}})^2 + (\bar{C}_{12}^{\text{H}})^2 \right) (\bar{C}_{11}^{\text{H}})' - 2\bar{C}_{11}^{\text{H}} \bar{C}_{12}^{\text{H}} (\bar{C}_{12}^{\text{H}})'}{(\bar{C}_{11}^{\text{H}})^2} \quad (\text{D.20e})$$

$$\frac{\partial \nu}{\partial z_i} = \frac{(\bar{C}_{12}^{\text{H}})' \bar{C}_{11}^{\text{H}} - \bar{C}_{12}^{\text{H}} (\bar{C}_{11}^{\text{H}})'}{(\bar{C}_{11}^{\text{H}})^2} \quad (\text{D.20f})$$

$$\frac{\partial \bar{\rho}}{\partial z_i} = \frac{V'}{V_0} \quad (\text{D.20g})$$

where $\bar{C}_{11}^{\text{H}} = \frac{1}{2}(C_{11}^{\text{H}} + C_{22}^{\text{H}})$.

D.2. Sensitivity analysis of the constraints

Both the isotropy and stiffness constraints depend on the design variables through the homogenized constitutive matrix, $\mathbf{C}^{\text{H}}(\mathbf{z})$, which is defined in Eq. (7). Pleasantly, the sensitivity of the homogenized constitutive matrix can be computed as

$$\frac{\partial \mathbf{C}^{\text{H}}}{\partial z_i} = \frac{1}{S_{\text{uc}}} \mathbf{D}_e^T \frac{\partial \mathbf{K}_{\text{uc}}(\mathbf{z})}{\partial z_i} \mathbf{D}_e \quad (\text{D.21})$$

which enables the sensitivities of the constraint functions, g_E and g_{iso} , to be computed using elementary rules of differentiation and no additional FE analysis (Sigmund and Torquato, 1997). Thus, the full derivations are excluded here for brevity.

Data availability

Data will be made available on request.

References

- Bendsoe, M.P., 1989. Structural optimization optimal shape design as a material distribution problem. *Struct. Optim.* 1, 193–202. <http://dx.doi.org/10.1007/BF01650949>.
- Cook, R.D., Malkus, D.S., Plesha, M.E., Witt, R.J., 2002. *Concepts and Applications of Finite Element Analysis*, fourth ed. John Wiley & Sons.
- Da, D., Qian, X., 2020. Fracture resistance design through biomimicry and topology optimization. *Extrem. Mech. Lett.* 40, <http://dx.doi.org/10.1016/j.eml.2020.100890>.
- Fleck, N.A., Qiu, X.M., 2007. The damage tolerance of elastic-brittle, two-dimensional isotropic lattices. *J. Mech. Phys. Solids* 55, 562–588. <http://dx.doi.org/10.1016/j.jmps.2006.08.004>.
- Gupta, S., Moini, R., 2024. Tough cortical bone-inspired tubular architected cement-based material with disorder. *Adv. Mater.* <http://dx.doi.org/10.1002/adma.202313904>.
- Hsieh, M.T., Deshpande, V.S., Valdevit, L., 2020. A versatile numerical approach for calculating the fracture toughness and R-curves of cellular materials. *J. Mech. Phys. Solids* 138, <http://dx.doi.org/10.1016/j.jmps.2020.103925>.
- Jia, Y., Lopez-Pamies, O., Zhang, X.S., 2023. Controlling the fracture response of structures via topology optimization: From delaying fracture nucleation to maximizing toughness. *J. Mech. Phys. Solids* 173, 105227. <http://dx.doi.org/10.1016/J.JMPS.2023.105227>.
- Lipperman, F., Ryvkin, M., Fuchs, M.B., 2007. Nucleation of cracks in two-dimensional periodic cellular materials. *Comput. Mech.* 39, 127–139. <http://dx.doi.org/10.1007/s00466-005-0014-9>.
- Lipperman, F., Ryvkin, M., Fuchs, M.B., 2008. Crack arresting low-density porous materials with periodic microstructure. *Internat. J. Engrg. Sci.* 46, 572–584. <http://dx.doi.org/10.1016/j.ijengsci.2008.01.004>.
- Lipperman, F., Ryvkin, M., Fuchs, M.B., 2009. Design of crack-resistant two-dimensional periodic cellular materials. *J. Mech. Mater. Struct.* 4, 441–457. <http://dx.doi.org/10.2140/jomms.2009.4.441>.
- Mane, S.M., Liechti, K.M., Huang, R., 2024. A numerical study on tensile strength of low-density kagome networks made of brittle fibers. *Int. J. Solids Struct.* 302, <http://dx.doi.org/10.1016/j.ijsolstr.2024.112987>.
- Maurizi, M., Edwards, B.W., Gao, C., Greer, J.R., Berto, F., 2022. Fracture resistance of 3D nano-architected lattice materials. *Extrem. Mech. Lett.* 56, 101883. <http://dx.doi.org/10.1016/J.EML.2022.101883>.
- Omidi, M., St-Pierre, L., 2023a. The fracture toughness of demi-regular lattices. *Scr. Mater.* 237, <http://dx.doi.org/10.1016/j.scriptamat.2023.115686>.
- Omidi, M., St-Pierre, L., 2023b. Fracture toughness of semi-regular lattices. *Int. J. Solids Struct.* 270, <http://dx.doi.org/10.1016/j.ijsolstr.2023.112233>.
- Quintana-Alonso, I., Fleck, N.A., 2010. Fracture of brittle lattice materials: A review. In: Daniel, I., Gdoutos, E., Rajapakse, Y. (Eds.), *Major Accomplishments in Composite Materials and Sandwich Structures*. pp. 799–816.
- Romijn, N.E., Fleck, N.A., 2007. The fracture toughness of planar lattices: Imperfection sensitivity. *J. Mech. Phys. Solids* 55, 2538–2564. <http://dx.doi.org/10.1016/j.jmps.2007.04.010>.
- Shaikheea, A.J.D., Cui, H., O'Masta, M., Zheng, X.R., Deshpande, V.S., 2022. The toughness of mechanical metamaterials. *Nat. Mater.* 21, 297–304. <http://dx.doi.org/10.1038/s41563-021-01182-1>.
- Sigmund, O., 2007. Morphology-based black and white filters for topology optimization. *Struct. Multidiscip. Optim.* 33, 401–424. <http://dx.doi.org/10.1007/s00158-006-0087-x>.
- Sigmund, O., Torquato, S., 1997. Design of materials with extreme thermal expansion using a three-phase topology optimization method. *J. Mech. Phys. Solids* 45, 1037–1067.
- Svanberg, K., 1987. The method of moving asymptotes—a new method for structural optimization. *Internat. J. Numer. Methods Engrg.* 24, 359–373. <http://dx.doi.org/10.1002/nme.1620240207>.
- Tankasala, H.C., Deshpande, V.S., Fleck, N.A., 2015. 2013 koiter medal paper: Crack-tip fields and toughness of two-dimensional elastoplastic lattices. *J. Appl. Mech. Trans. ASME* 82, <http://dx.doi.org/10.1115/1.4030666>.
- Vigliotti, A., Pasini, D., 2012. Linear multiscale analysis and finite element validation of stretching and bending dominated lattice materials. *Mech. Mater.* 46, 57–68. <http://dx.doi.org/10.1016/j.mechmat.2011.11.009>.